

Small particles and self-gravity wakes in Saturn's rings from UVIS and VIMS stellar occultations



Richard G. Jerousek^{a,*}, Joshua E. Colwell^a, Larry W. Esposito^b, Philip D. Nicholson^c, Matthew M. Hedman^d

^a Department of Physics and Florida Space Institute, University of Central Florida, Orlando, FL 32816, USA

^b Laboratory for Atmospheric and Space Physics, University of Colorado, Boulder, CO 80309, USA

^c Department of Astronomy, Cornell University, Ithaca, NY 14853, USA

^d Department of Physics, University of Idaho, Moscow, ID 83844, USA

ARTICLE INFO

Article history:

Received 22 January 2016

Revised 19 April 2016

Accepted 25 April 2016

Available online 11 May 2016

Keywords:

Saturn, rings

Photometry

Resonances, orbital

ABSTRACT

The distribution of particle sizes in Saturn's rings roughly follows a truncated inverse power-law. Though it is well known that differential optical depths provide a way to probe the parameters of size distribution (i.e. Zebker et al. [1985] *Icarus*, 64, 531–548), the technique is complicated by the presence of self-gravity wakes which introduce a geometric dependence to the observed optical depth. Here we present a method of extracting information about the size distribution of the particles in the gaps between the self-gravity wakes. The Cassini Visual and Infrared Mapping Spectrometer (VIMS) occultations measure starlight at an effective wavelength of 2.9 μm falling onto a single pixel with angular dimensions 0.25 mrad × 0.5 mrad while Cassini Ultraviolet Imaging Spectrograph (UVIS) occultations measure starlight at a much smaller effective wavelength of 0.15 μm and over a field of view with larger angular dimensions of 6.0 mrad × 6.4 mrad. Starlight diffracted out of the VIMS pixel by particles smaller than $1.22\lambda_{\text{VIMS}}/2\theta \sim 8.86$ mm, is not replaced by neighboring particles, while the UVIS instrument, with its larger field of view and smaller effective wavelength, collects all of the light diffracted by particles larger than $1.22\lambda_{\text{VIMS}}/2\theta \sim 0.025$ mm. Consequently, measurements by VIMS overstate the optical depth in regions where sub-centimeter-sized particles are present. Using the rectangular cross section wake model of (Colwell et al. [2006], *Geophys. Res. Lett.*, 33, L07201) and (Colwell et al. [2007] *Icarus*, 190, 127–144) with a new parameter to represent the excess VIMS optical depth not seen by UVIS, we combine VIMS and UVIS occultations for the first time for particle size analysis. We find a significant fraction of sub-cm particles only in the outermost portion of the A ring, and in the B1 region of the B ring. In the Trans-Encke region, we find a trend of increasing abundance of sub-cm particles as the outer edge of the A Ring is approached, consistent with previous differential optical depth studies at radio wavelengths (Zebker et al. [1985] *Icarus*, 64, 531–548), measurements of diffraction in stellar occultations at the ring edges (Becker et al. [2015] *Icarus*), and measurements from VIMS solar occultations (Habibou et al. [2013] *Icarus*, 226, 1225–1240). This may be due to greater erosion of weakly bound particle aggregates by interparticle collisions in regions where satellite perturbations are strong.

© 2016 Elsevier Inc. All rights reserved.

1. Introduction

The discrete particulate nature of Saturn's rings was first hypothesized by Maxwell, (1859). Since then, early Earth-based studies assumed a description of the ring plane as a many particle thick disk in which the number of particles, $n(a)da$, of a given radius a roughly follows an inverse power-law size distribution between

some minimum particle radius, a_{\min} and some maximum particle radius, a_{\max} :

$$n(a)da = n_0 \left(\frac{a}{a_0} \right)^{-q} da, \quad a_{\min} \leq a \leq a_{\max}. \quad (1)$$

where n_0 and q are assumed constants. Differential optical depth measurements provide one means of determining the parameters of the size distribution (Marouf et al., 1983; Zebker et al., 1985). Using Voyager 2 optical depth measurements at 13-cm (X band) and 3.6-cm (S band) as well as direct inversion of the forward scattered S band signal, Zebker et al. (1985) constrained the power-law parameters over the range of ~ 0.1 cm $< a < \sim 1.0$ m. Particles

* Corresponding author. Tel.: +1 4079021092.

E-mail address: RJerousek@gmail.com, RJerousek@ValenciaCollege.edu (R.G. Jerousek).

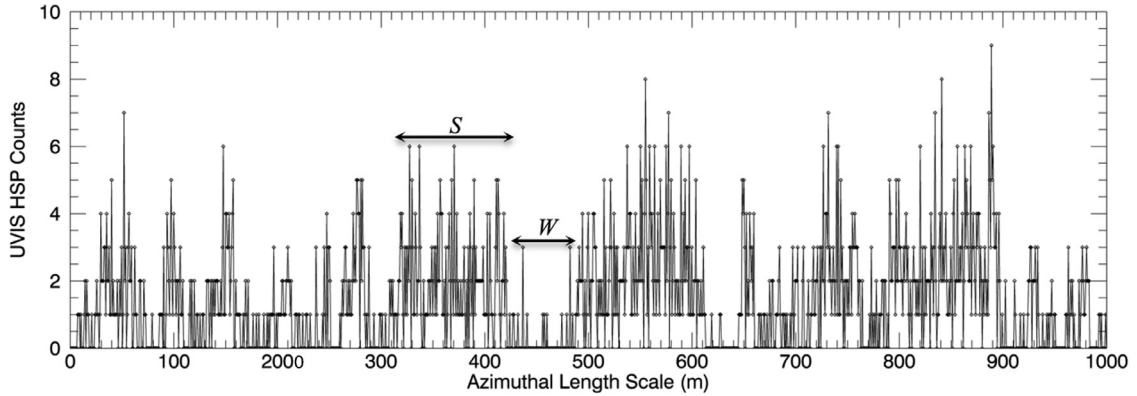


Fig. 1. The occultation of β -Persei (rev 116) when the relative velocity of the spacecraft with respect to the orbital velocity particles in the patch of the ring being observed reached its minimum value of ~ 0.81 km/s. The UVIS high-speed photometer (HSP) measured starlight passing through the ring plane at a 1.0 ms sampling rate. The figure shows the unbinned HSP data with 0.81 m azimuthal resolution and radial resolution of < 10 cm. The distribution of HSP counts shows what appear to be relatively opaque wakes and the more transparent gaps. The width of one wake is labeled “ W ”, and the width of the adjacent gap is labeled “ S ”. The figure shows a typical separation to width ratio (S/W) of ~ 1.7 at this location, 131,436 km from Saturn’s center.

smaller than ~ 0.1 cm are essentially invisible to even the smaller of the two wavelengths. Other attempts to constrain the parameters of the size distribution include measurements of excess variance beyond the Poisson statistics of the signal measured by Voyager PPS occultations (Showalter and Nicholson, 1990) and Cassini UVIS occultations (Colwell et al., 2011) as well as the results of ground-based measurements of the forward-scattered stellar flux from the 1989 occultation of 28 Sgr by Saturn’s rings (French and Nicholson 2000). More recently, Harbison et al. (2013) studied diffracted sunlight measured by VIMS finding a significant fraction of sub-mm particles if $q < 3.0$ while Becker et al. (2015) modeled the starlight diffracted by the sharp edges of Saturn’s many ringlets in an attempt to constrain both q and a_{\min} at the edges. They find that the size distribution parameters vary across the rings but that generally $q \sim 2.75\text{--}3.5$ with particle radii ranging between several millimeters and several meters. This range of q is also corroborated by models of particle aggregation and fragmentation in planetary ring systems (Brilliantov et al. 2015). While numerical simulations of adhesion and collisional release by Bodrova et al. (2012) predict an absence of sub-cm particles throughout the rings except in regions of increased velocity dispersion. Ground-based observations have suggested that the particle size distribution extends to smaller sizes in the trans-Encke region than it does anywhere else in the A ring (French and Nicholson 2000).

Determining particle sizes in Saturn’s rings is complicated by azimuthal brightness asymmetries found in Saturn’s A and B rings (Camichel, 1958; Colombo et al., 1976; Lumme and Irvine, 1976; Reitsema et al., 1976; Lumme et al., 1977; Gehrels and Esposito, 1981; Thompson et al., 1981; Dones and Porco, 1989; Dones et al., 1993; Dunn et al., 2004; Nicholson et al., 2005). These observations have since been explained by the presence of aligned trailing density enhancements (Julian and Toomre 1966) now known as self-gravity wakes (Colwell et al. 2006). In locations where the surface mass density is sufficiently high and the radial epicyclic frequency, κ , sufficiently small, ring particles clump together under their mutual self-gravity only to be torn apart by Keplerian shear, leaving the self-gravity wakes with a characteristic cant angle of $\sim 25^\circ$ from the direction of orbital motion. The most unstable wavelength for gravitational collapse, the Toomre critical wavelength, is given by

$$\lambda_{\text{crit}} = 4\pi^2 G\sigma/\kappa^2 \quad (2)$$

where σ is the local surface mass density (Julian and Toomre 1966). Estimates of local surface mass densities in Saturn’s rings give Toomre critical wavelengths significantly larger than individ-

ual ring particles only in the A and B rings where wavelengths range between $\sim 50\text{--}100$ m. This small spatial scale has mostly limited studies of self-gravity wake properties to indirect methods.

While the characteristic scale of self-gravity wakes is generally too small for direct observation, several UVIS occultations have a resolution in the frame co-orbiting with the ring particles of ~ 1 m or less at the minimum ring plane radius sampled by the occultation. In these occultations, the self-gravity wakes are resolved, though with a low signal-to-noise ratio (Fig. 1). Numerical simulations by (Salo et al. 1995, 2004) have demonstrated the presence of self-gravity wakes in simulated rings with surface mass densities similar to those of the A and B rings. Simulations by Salo et al. (2004) found that centimeter-sized particles were less effective at aggregating into wakes than meter-sized particles and therefore constitute a larger fraction of the material in the gaps between wakes. Salo et al. (2004) also found that simulated regions of the ring plane with more small particles tended to produce wakes with larger cant angles.

Self-gravity wake properties have been determined by comparing stellar occultation data at different viewing geometries (Colwell et al. 2006, 2007; Hedman et al. 2007; Nicholson and Hedman 2010). Colwell et al. (2006, 2007) modeled the wakes as infinitely long rectangular slabs in order determine wake optical depths as well as wake shape, orientation and interwake optical depths. The five parameter rectangular cross-section of this “granola bar” model was compared with a dozen stellar occultations and 1 solar occultation measured by the Cassini Ultraviolet Imaging Spectrograph (UVIS) and the δ -Scorpii occultation measured by Voyager PPS across the A and B rings in order to determine the best-fit parameters representing the height (H) and separation (S) of the wakes relative to the wake width (W), (H/W and S/W) as well as the orientation angle measured from the outward radial direction (φ_{wake}), and interwake and intrawake optical depths (τ_{gap} and τ_{wake}) (Fig. 2).

Hedman et al. (2007) modeled the wakes as infinitely long, opaque tubes with elliptic cross-section and compared the model with optical depth profiles from stellar occultations by the Cassini Visual and Infrared Mapping Spectrometer (VIMS). Four occultations of the star Omicron Ceti at the extremely low occultation elevation angle, $B = 3.5^\circ$, allowed the wake orientation relative to the outward radial direction from Saturn, φ_{wake} , to be determined independent of any geometric model of the wakes by fitting the measured ring plane transparencies at a given radial location to a Gaussian distribution throughout much of the A ring. Both approaches found that generally the wakes are canted by

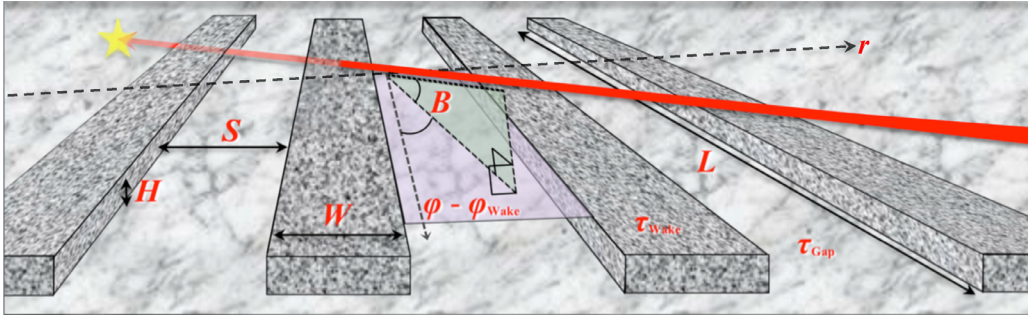


Fig. 2. A schematic model patch of the rings illustrating the free parameters of the rectangular cross-section “granola bar” model of (Colwell et al. 2006). In our new analytic model we have $L = \infty$, $\tau_{\text{wake}} = \infty$ (cf. Colwell et al. 2007), and an additional free parameter τ_{small} (see text) represents the over-prediction of τ_{gap} by VIMS occultations. The line-of-sight from Cassini to the star makes an angle of B with the ring plane, while the wakes make an angle of φ_{wake} counterclockwise from the radial direction outward from Saturn, r , toward the trailing orbital direction.

~20–25° from the direction of orbital motion consistent with the gravitational instability model for self-gravity wakes in a Keplerian disk (Salo et al. 2004). Further studies by Nicholson and Hedman (2010) compared the elliptical cross-section, or “pasta” model (in keeping with the culinary naming theme), to occultations that cut across the wakes at right angles, determining separation relative to their characteristic wavelength (G/λ), height to wavelength ratio (H/λ), and interwake optical depth (τ_{gap}). G is the average distance between wakes and is equivalent to S in the granola bar model. The granola bar model of Colwell et al. (2006) and pasta model of Hedman et al. (2007) results are inherently difficult to compare due to differences in the geometry of the simplified self-gravity wakes. For example, the height determined by using the rectangular cross-section is not the same as the height determined for the elliptic cylinders and this difference will propagate to differences in the other wake parameters in order to reproduce the same optical depth at a given viewing geometry. Secondly, the particular set of optical depth profiles that were used to fit the model parameters were measured by one of two different instruments, VIMS and UVIS, which measure light at different effective wavelengths and which have measured stellar occultations with dissimilar distributions of viewing angles across the rings.

In this paper, we combine UVIS and VIMS stellar occultation measurements with a geometric model of the self-gravity wakes to enable us to extract information about the particle size distribution from the optical depths at two wavelengths. The differences in optical depth measurements at different viewing geometries due to self-gravity wakes are much larger than those due to the different wavelengths of observations. Thus we must fold the differential optical depth of the two instruments into a model of the self-gravity wakes. In Section 2 we describe the observations used in the study. In Section 3 we describe the mechanism by which we can extract particle size information by eliminating the geometric effects of the self-gravity wakes from the VIMS and UVIS measurements and the modified self-gravity wake model for this study. We further find that the structure of self-gravity wakes in the A and B rings are qualitatively different, with those in the A ring clearly separated by relatively empty gaps with optical depth ~0.1, while those in the B ring have less-well-defined gaps with higher optical depths. We present our results on self-gravity wake parameters across the A and B rings, including particle sizes extracted from the comparison of VIMS and UVIS occultations, in Section 4. We discuss the implications of our results and next steps in Section 5.

2. Observations

UVIS observed 128 stellar occultations between May 21st, 2005 and July 9th, 2013, with its High-speed Photometer (HSP) and over 58 stellar occultations were observed by the Visual and Infrared

Mapping Spectrometer (VIMS) between May, 24th 2005 and July 25th, 2010. Each of these occultations measured a one-dimensional trace of the intensity of starlight passing through the rings over a wide range of radii and azimuthal viewing angles. In order to compare measured intensities between occultations, the geometry of the occultations (the ring plane radius, r , measured outward from Saturn’s center, the occultation elevation angle, B (Fig. 2), measured from the ring plane to the line-of-sight to the star, and the ring plane azimuth angle, φ (Fig. 2), measured from the outward radial direction from Saturn to the ring plane projection of the line-of-sight from Cassini to the star) must be calculated (Colwell et al. 2006). These geometric parameters were determined using the Navigation and Ancillary Information Facility’s (NAIF) SPICE toolkit as outlined in Colwell et al. (2010).

The measured normal optical depth is given by

$$\tau_N = \mu \ln\left(\frac{1}{T}\right) = \mu \ln\left(\frac{I_0}{I(t) - b}\right) \quad (3)$$

where $\mu = \sin|B|$, T is the transparency of the rings, $I(t)$ is the total measured signal, I_0 is the unocculted star signal and b is the contribution of background signal primarily due to ring shine and, in the case of UVIS, Lyman- α emission from interplanetary hydrogen. Details on the determination of I_0 and b are also outlined in Colwell et al. (2010). Background signal, b , is negligible in VIMS occultations due to the proximity of the measured wavelength to a strong water ice absorption band (Hedman et al. 2007). Detailed descriptions of the instruments and measurement modes can be found in Esposito et al. (2004) (UVIS) and Brown et al. (2004) (VIMS). Below we summarize the salient features for this analysis.

The Ultraviolet Imaging Spectrograph. The Ultraviolet Imaging Spectrograph (UVIS) high-speed photometer (HSP) measures starlight over the wavelength range from 110–190 nm incident upon the 6.0×6.4 mrad field of view. Here, we use an effective wavelength of 150 nm. This gives a critical particle size of $a_{\text{crit}} = 1.22\lambda_{\text{UVIS}}/2\theta \sim 0.025$ mm below which diffraction effects become important. The UVIS HSP has measured 128 ring stellar occultations as of July 9, 2013, and 100 of those were included in this study, and are listed in Table A.1. The occultations that were not included had one or more of the following issues: high uncertainties in I_0 and/or b , limited geometric coverage of the rings, and a low star signal. The occultations span a large range of viewing geometries, with ring-plane opening angles, B , ranging from 2.3° to 66° and φ spanning 360° over the entire set of occultations. While B is fixed for a given star, φ varies over the course of each occultation. Integration times are 1 or 2 ms for all occultations included in this study giving a radial sampling interval of < 30 m. However in this study data are binned to 10 km in ring plane radius in order

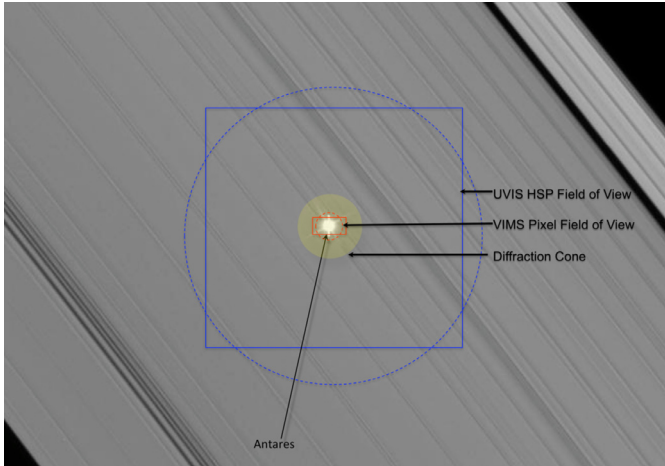


Fig. 3. The rectangular pixel of angular dimensions 0.25×0.5 mrad of the VIMS instrument (red) and the nearly square UVIS field of view of angular dimensions 6.0×6.4 mrad (blue). During stellar occultations, $2.9 \mu\text{m}$ light diffracted out of the VIMS pixel is not replaced by light diffracted by neighboring particles. The much larger field of view and smaller effective wavelength of the UVIS HSP ($0.15 \mu\text{m}$) place the entirety of the diffraction cone within the field of view for particles larger than $25 \mu\text{m}$ in radius. The background image is the January 3rd, 2008 occultation of the star Antares (α -Scorpii) by the outer A ring (NASA/JPL-Caltech/Space Science Institute) captured by the narrow-angle camera from an angle of 34° above the ring plane at a distance of 541,000 km. The relative sizes of the VIMS and UVIS field of view (FOV) are accurate, however the sizes of the two FOVs are not to scale with the background image at the distance of the spacecraft from the rings during the time the image was taken. (For interpretation of the references to color in this figure legend, the reader is referred to the web version of this article).

to increase the signal to noise ratio and provide a uniform radial sampling between occultations.

The Visual and Infrared Mapping Spectrometer. In stellar occultation mode, the Visual and Infrared Mapping Spectrometer (VIMS) collects stellar spectra from $0.8\text{--}5.1 \mu\text{m}$ incident on a single rectangular pixel of angular dimensions 0.25×0.5 mrad. Stellar occultation measurements collected light over the band from $\sim 2.87\text{--}3.0 \mu\text{m}$, with an effective wavelength of $2.9 \mu\text{m}$ due to this wavelength band's proximity to the strong water ice absorption feature (Hedman et al. 2007; Brown et al. 2004). This reduces background signal due to sunlight reflected from the rings. The longer measured wavelength and smaller angular dimensions of the VIMS field of view compared with UVIS give a much larger critical particle radius of $a_{\text{crit}} = 1.22\lambda_{\text{VIMS}}/2\theta_{\text{eff}} \sim 8.86 \text{ mm}$ below which diffraction effects become important (Fig. 3). We use an effective circular aperture radius of $\theta_{\text{eff}} = (L \times W/\pi)^{1/2}$ where L and W represent the angular dimensions of the rectangular field of view of the instrument. During stellar occultations measured by VIMS, the star must be centered within the pixel prior to the occultation of the ring plane. Therefore, occultations are either ingress occultations or chord occultations with both ingress and egress radial samplings. In 25 occultation profiles the unocculted star signal showed a strong temporal variability in brightness indicating the star did not remain centered within a single pixel. We did not include these occultations in this study due to the additional uncertainty in measured optical depth. 44 VIMS occultations were used and are listed in Table A.1. VIMS occultations spanned ring opening angles between $2.3^\circ < B < 72^\circ$ and $0^\circ < \varphi < 360^\circ$ over the entire range of occultations. VIMS integration times are typically $\sim 80 \text{ ms}$ giving a typical radial sampling of $\sim 1.3 \text{ km}$ but in this study the data were binned to 10 km radial resolution for uniformity with the binned UVIS occultations.

Effect of particle size distribution on measured optical depth

The effect of the presence of particles smaller than $\sim 8.86 \text{ mm}$ in the ring plane results in normal optical depths measured by

VIMS that would be larger than those measured by UVIS at the same viewing geometry. To illustrate this point we refer to one of the handful of occultations that were conducted simultaneously by both the VIMS and UVIS instruments.

Antares, a binary star system with a small angular separation of $\sim 3.3''$ and spectral classes of M1.5I (Antares A, bright in IR) and B2.5 (Antares B, bright in UV) has been observed by VIMS and UVIS on multiple Cassini orbits or “revs”. The line-of-sight to Antares (α -Scorpii) from Cassini cut a chord across the rings on the rev 13 observation (Fig. 4). The in-going (ingress) and out-going (egress) sections of the chord occultation provide two independent radial measurements of optical depth for each instrument at each radial distance from Saturn and at two significantly different ring plane azimuthal angles, φ , and therefore at significantly different viewing geometries with respect to the self-gravity wakes. There is a significant difference in optical depth between the ingress and egress sections of the occultation due to the different viewing geometry with respect to the elongated self-gravity wakes. When the line of sight to the star is more aligned with the self-gravity wake orientation, more starlight passes through the ring and the optical depth is lower (Fig. 4, Egress), while when the line of sight is more orthogonal to the wakes, the gaps are shadowed by the wakes, less starlight gets through and the measured optical depth is higher (Fig. 4, Ingress). The fractional difference in optical depth for each section (ingress or egress) of the α -Scorpii occultation, however, is only due to the diffraction of light out of the small VIMS pixel by sub-cm particles. The VIMS optical depths are higher than UVIS throughout the α -Scorpii occultation, though the effect is more pronounced in the outer A ring and in the (Ingress) branch of the occultation.

In general, however, VIMS and UVIS occultations are of different stars at very different ring elevation angles, B , and azimuthal angles φ , (Fig. 5). Thus the effect of self-gravity wakes must be accounted for before particle size information can be extracted from the full collection of VIMS and UVIS occultations. In the next section we describe combining the multiple optical depth measurements from UVIS and VIMS with a model of the wake properties and the effects of small particle diffraction.

3. Model

The dependence of the apparent measured normal optical depth on wavelength is a result of light diffracted out of the instrument's field of view that is not replaced by light diffracted by neighboring particles. The classical expression for the optical depth of a cloud of particles with size distribution $n(a)da$ is

$$\tau = \int_{a_{\min}}^{a_{\max}} \pi a^2 Q_e(a, \lambda) n(a) da \quad (4)$$

where Q_e , the extinction efficiency, is a function of the particle radius, a , and the wavelength of collected light, λ . If $\lambda \ll a$, then the light blocked by the particles is proportional to the fractional area that is blocked by the particles. An equal amount of light is diffracted by the particles, and in the case where the diffracted light can be distinguished from the incident beam, such as in radio occultations with a coherent signal, then $Q_e = 2$. For stellar occultations where the diffraction angle is small ($\lambda \ll a$), the diffracted signal is generally indistinguishable from the incident beam and $Q_e = 1$. This accounts for the familiar factor of two difference between radio occultation optical depths from both Voyager and Cassini and those from stellar occultations such as UVIS, VIMS, and the Voyager PPS (Cuzzi (1985); French and Nicholson (2000)). If $\lambda \gg a$ leading to larger diffraction angles and/or if the field of view is small, then the diffracted light is not all collected by the instrument and Q_e approaches 2. Due to the large field of view and smaller effective wavelength of UVIS $Q_e = 1$ for all particles of $a > 0.025 \text{ mm}$

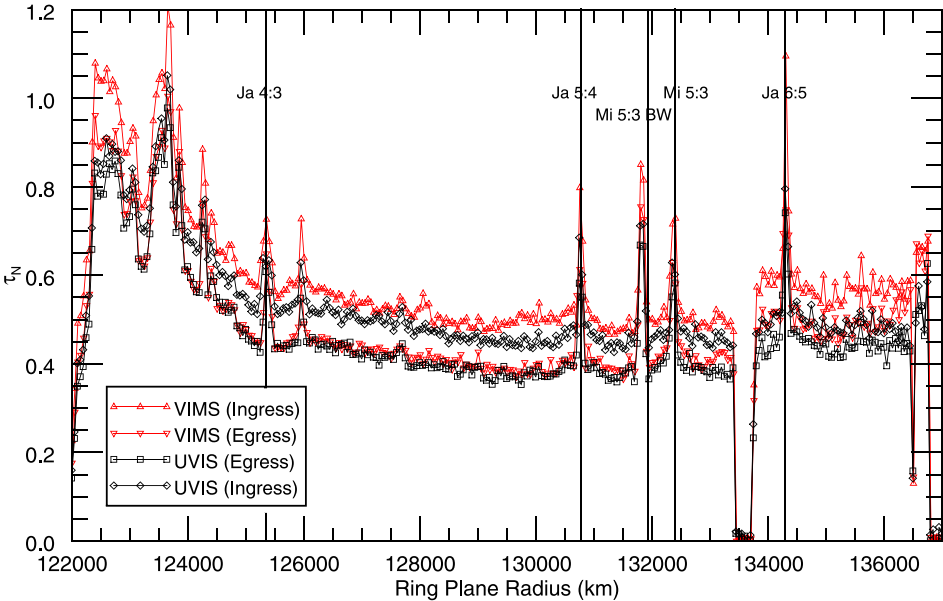


Fig. 4. The α -Scorpii A,B (rev 13) occultation with simultaneous observations by both VIMS and UVIS. These occultation profiles, which cut a chord across the rings, illustrate the geometry and wavelength dependence of measured normal optical depth. The difference in measured normal optical depth between ingress and egress for either VIMS (Red) or UVIS (Black) illustrates the geometry dependence imposed on measured normal optical depth by the presence of self-gravity wakes. The difference in optical depth between VIMS (Red) and UVIS (Black) in either ingress or egress sections is due to diffraction of light out of the VIMS field of view by small particles within the rings. The strongest resonances with the moons Janus and Mimas are demarcated with dashed lines. Antares A was not centered within the VIMS pixel during the rev 13 occultation leading to large systematic errors in measured optical depth. Therefore we did not include the VIMS occultation of α -Scorpii A (rev 13) in the study and merely use these simultaneous occultations to illustrate the effects of viewing geometry and wavelength on the measured optical depth. (For interpretation of the references to color in this figure legend, the reader is referred to the web version of this article).

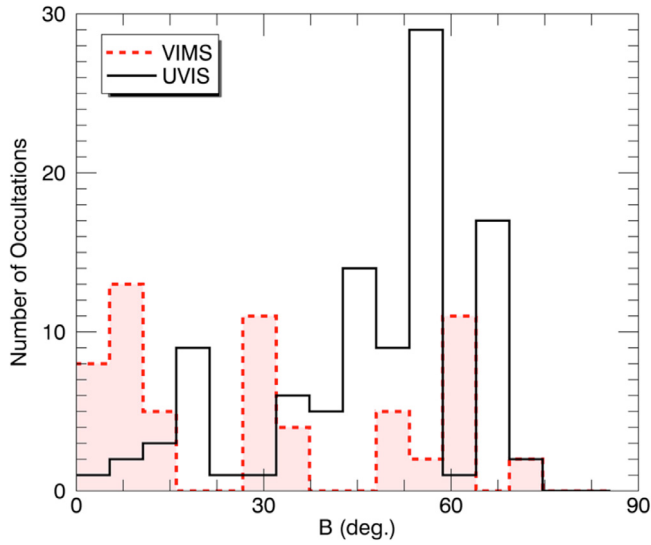


Fig. 5. Distribution of stellar elevation angles, B , from the ring plane for VIMS and UVIS occultations.

because the diffraction cone subtends a small solid angle, and virtually all of the diffracted light is captured within the field of view:

$$\tau_{UVIS} = 1 \cdot \frac{\pi n_0}{a_0^{-q}} \int_{a_{min}}^{a_{max}} a^{2-q} da = \pi n_0 a_0^q \left[\frac{(a_{max}^{3-q} - a_{min}^{3-q})}{3-q} \right] \quad (5)$$

for a power law size distribution with respective upper and lower cutoff radii of a_{max} and a_{min} . For VIMS, on the other hand, with a wavelength of 2.92 μm for ring stellar occultations and a much smaller field of view, the critical particle radius below which Q_e essentially transitions from 1 to 2 is ~ 8.86 mm. Approximating Q_e

as either 1 or 2, the VIMS optical depth is then

$$\begin{aligned} \tau_{VIMS} &= \frac{\pi n_0}{a_0^{-q}} \left[2 \cdot \int_{a_{min}}^{a_{crit}} a^{2-q} da + 1 \cdot \int_{a_{crit}}^{a_{max}} a^{2-q} da \right] \\ &= \pi n_0 a_0^q \left[\frac{(a_{max}^{3-q} + a_{crit}^{3-q} - 2a_{min}^{3-q})}{3-q} \right]. \end{aligned} \quad (6)$$

Therefore, in the absence of self-gravity wakes, the additional apparent optical depth measured by VIMS due to diffraction of light out of the field of view is $\tau_{Small} = \tau_{VIMS} - \tau_{UVIS}$. The radius of the smallest particle in the assumed power-law size distribution can then be retrieved from τ_{Small} :

$$a_{min} = \left(a_{crit}^{3-q} - \frac{(3-q)a_0^{-q}}{\pi n_0} \tau_{Small} \right)^{\frac{1}{3-q}}. \quad (7)$$

When the slope of the power-law size distribution, q , is equal to three, the minimum particle size is given by:

$$a_{min} = a_{crit} \cdot \exp \left(- \frac{\tau_{Small}}{\pi n_0 a_0^3} \right). \quad (8)$$

In an attempt to understand the relative differences in normal optical depths between and within the self-gravity wakes, we used a ray-tracing scheme and the rectangular cross-section “granola bar” model of Colwell et al. (2006, 2007). In this model, infinitely long parallel rectangular wakes uniquely determine the observed transparency as a function of five parameters: the height to width ratio of the wakes, H/W , the separation to width ratio, S/W , the orientation of the wakes from the outward radial direction from Saturn toward the trailing orbital direction, φ_{Wake} , and the optical depths of both the wakes and the gaps between them, τ_{wake} and τ_{gap} (Fig. 2). The ray-tracing scheme integrates the differential extinction of starlight along the line-of-sight to the spacecraft due to a simulated patch of the rings and compares the model computed transparency, T_{Comp} to the transparencies measured by stellar

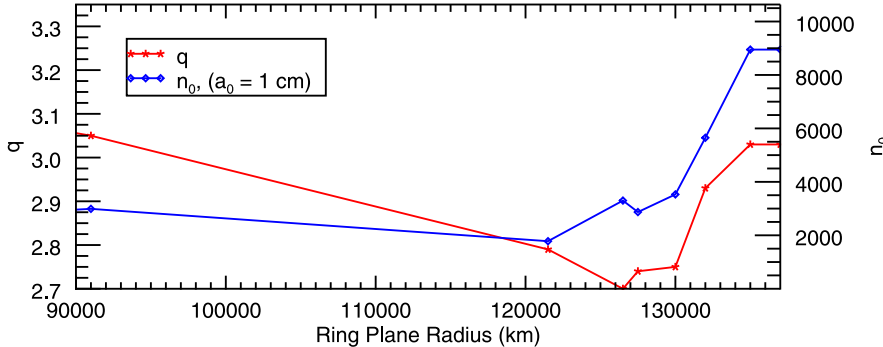


Fig. 6. Slope of the power-law particle size distribution, q , and number of 1 cm particles, n_0 , determined by (Zebker et al. 1985) from Voyager Radio Science Subsystem differential optical depths. q (red line) and n_0 (blue line) are determined at each radial location by interpolating between data points given in (Zebker et al. 1985). (For interpretation of the references to color in this figure legend, the reader is referred to the web version of this article).

occultations, T_{Measured} , for a wide range of the various wake parameters.

We modeled the VIMS occultations and separately, the UVIS occultations using the original five-parameter ray-tracing model of (Colwell et al. 2006) and the multitude of occultation profiles included in this study and determined that the best-fit wake optical depths throughout the A and B ring are $\tau_{\text{wake}} \sim 4$. Optical depths of ~ 4 (transparency ~ 0.02) are lower limits in this model: the model and data cannot distinguish wake optical depths of 4 from higher values. We conclude that the wakes are essentially opaque to both the 0.15 and 2.9 μm wavelengths observed by UVIS and VIMS respectively and we eliminate the free parameter τ_{Wake} . The elimination of τ_{Wake} allows us to use an analytic solution for the expected transparency of the ring in terms of the remaining wake parameters (Colwell et al. 2007).

Using the analytic expression for the transparency as a function of the aforementioned wake parameters from Colwell et al. (2007), we introduce an additional free parameter, τ_{Small} (Eq. (7)) representing the apparent additional optical depth measured by VIMS occultations due to the diffraction of light out of the VIMS field of view by the small particle population in the gaps between the self-gravity wakes. Thus, the model predicts the optical depth of a patch of the rings, which depends on the properties of the self-gravity wakes (due to the particular viewing geometry of the occultation), as well as the particle size distribution (due to the particular wavelength and field-of-view size of the instrument.) Based on the results of the ray-tracing model, we treat the wakes as opaque and derive an analytic expression for the transparency of a patch of the ring plane:

$$T = \frac{S/W - H/W |\sin(\phi - \phi_{\text{Wake}})| \cot(B)}{S/W + 1} e^{-(\tau_{\text{Gap}} + \{\tau_{\text{Small}}, 0\})/\mu} \quad (9)$$

where the only difference from the corresponding expression in Colwell et al. (2007) is the inclusion of τ_{Small} at the viewing geometries of the VIMS occultations in the exponential term representing the attenuation of the stellar signal due to particles between the wakes. We combine both VIMS and UVIS transparencies in the model to find the best-fit wake parameters. In this “combined model”, the free parameter, τ_{Small} is set to zero for those viewing geometries corresponding to occultations measured by UVIS. Eq. (9) predicts the transparency at the viewing geometry of a single occultation based on the best-fit wake parameters. The resultant predicted normal optical depth can be found from $\tau_N = -\mu \ln(1/T)$.

τ_{Small} is directly related to the minimum particle size in the truncated power-law size distribution through Eq. (7). We get the slope of the power law distribution, q , by linear interpolation of the results from Voyager Radio Science Subsystem (Zebker et al. 1985) and Voyager Photopolarimeter Subsystem

(Showalter and Nicholson 1990) at various radial locations in the A and B rings. The particular values of q and n_0 at each radial location are shown in Fig. 6. The comparison of the two different wavelengths from only two instruments does not allow us to fit q as another free parameter; however additional occultations at other wavelengths could allow q to be incorporated into the model as another independent parameter. This is planned for future work.

Determination of best-fit parameters

The best-fit model parameters are determined by minimizing the root-sum of squared fractional differences in transparency:

$$\text{RSS} = \sqrt{\sum^N \left(\frac{T_{\text{Comp}} - T_{\text{Measured}}}{T_{\text{Comp}}} \right)^2} \quad (10)$$

Where N is the number of occultations covering the particular radial location in the rings. T_{Measured} represents a particular measured transparency and T_{Comp} is the model predicted transparency at the particular B and φ angles of the line-of-sight in the corresponding measured optical depth profile. The $1-\sigma$ error in transparency, T , due only to counting statistics and not the systematic errors in modeling I_0 and b is outlined in Colwell et al. (1990) and is given by:

$$\Delta T_{\text{UVIS}} = \sqrt{\frac{I}{n \cdot I_0}} \quad (11)$$

for UVIS occultations. I is the measured signal, I_0 is the unocculted star signal and n is the number of samples per radial bin. For VIMS, with its onboard analog to digital converter, the noise is dominated by read noise and detector dark current and is independent of the occultation mean signal level. In occultation mode, the VIMS data number is summed over 8 spectral channels. Thus the noise is independent of the mean signal, I , leading to:

$$\Delta T_{\text{VIMS}} = \sqrt{\frac{8}{n \cdot N_0}}, \quad (12)$$

where n_0 is the mean data number of the unocculted star signal. One data number represents ~ 300 photon counts. Statistical errors in transparency are typically on the order of ~ 0.02 for UVIS occultations and ~ 0.01 for VIMS occultations. In our determination of the best-fit model parameters, occultation transparencies were not weighted by their individual residuals. This is in part because occultations with low signal-to-noise ratios are at lower B angles and thus, their measured transparencies are more indicative of the height, separation, and orientation of the self-gravity wakes. For example, the large number of UVIS occultations of the bright star β -Centauri at the relatively high ring opening angle of $B = 66.2^\circ$

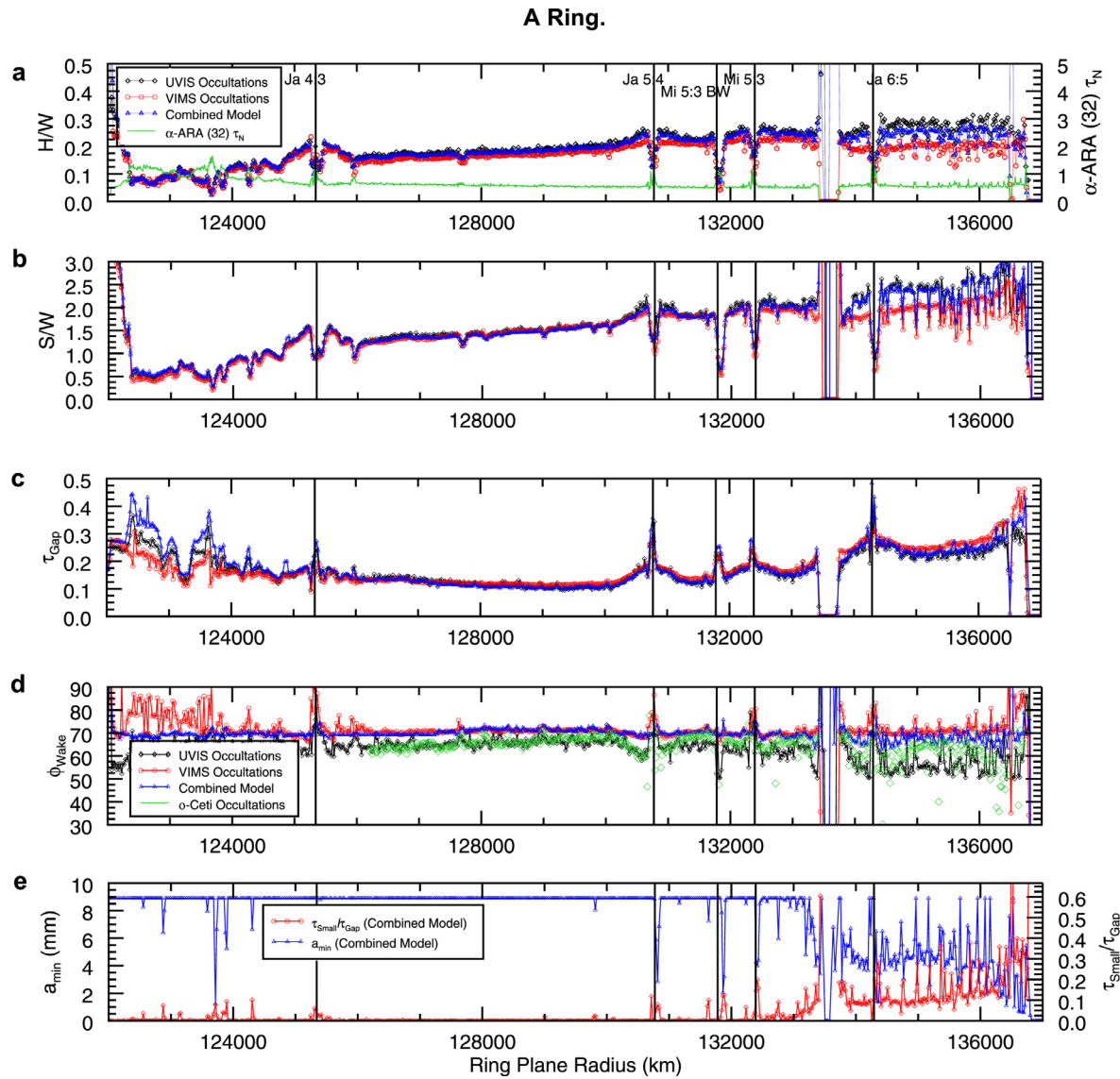


Fig. 7. (a,b,c) Best-fit wake height and separation to width ratios (H/W , S/W) and gap optical depth τ_{gap} throughout the A Ring. The difference in gap optical depths between VIMS and UVIS is due to the diffraction of light by sub-cm particles. (d) Best-fit φ_{Wake} from the granola bar models (black, red, and blue) as well as φ_{Wake} determined by fitting the measured transparency of the low B angle ($\sim 3.5^\circ$) occultations of o-Ceti by VIMS to a Gaussian at each radial location (green diamonds). (Hedman et al. 2007) VIMS measured five occultations of o-Ceti at various longitudes at each ring plane radius. (e) Best-fit τ_{Small} and the corresponding minimum particle size, a_{min} , throughout the A Ring which is dominated by self-gravity wakes. The radii of the smallest particles decreases toward the outer edge of the A Ring. From 122,000 km – 129,000 km we do not detect a significant population of sub-cm particles. (For interpretation of the references to color in this figure legend, the reader is referred to the web version of this article).

have a high signal-to-noise ratio, but at $B > 60^\circ$, they show virtually no dependence of the measured transparency on the wake orientation angle, φ_{Wake} . Therefore the weighing of the occultations on their statistical errors would preferentially select model parameters which fit the multitude of β -Centauri occultations with the same ring opening angle, B , well, but other, lower signal-to-noise occultations with different ring opening angles poorly. Also, systematic errors in the determination of I_0 , the unocculted star signal, and b , the background signal, are likely to be larger than the statistical error in transparency. Note, we report χ^2 (Fig. 11) using the best-fit parameters which were determined by minimizing the root-sum of squared fractional differences in transparency (RSS). χ^2 was calculated by weighing the differences in model computed and measured transparency by the $1-\sigma$ uncertainty due to photon counting statistics, ΔT :

$$\chi^2 = \frac{1}{v} \sum^N \left(\frac{T_{Comp} - T_{Measured}}{\Delta T} \right)^2. \quad (13)$$

v is the number of degrees of freedom (the number of occultations, N , at a given radial location less the number of free model parameters minus 1).

4. Results

A ring best-fit parameters

Results for the self-gravity wake aspect ratio (H/W) and separation (S/W) are shown with the gap optical depth in Fig. 7 (a and b) where we include results of fitting only the UVIS occultations, only the VIMS occultations, and the results of using our merged model taking diffraction into account. The model determined $S/W \sim 1.7$ at a radial distance of $\sim 131,400$ km from Saturn's center, consistent with particle-tracking occultation observations of resolved wakes in this region (Fig. 1). For all of the wake parameters, the differences in the results are largest in the inner A ring (interior to the Janus 4:3 inner Lindblad resonance) and in the outer A ring

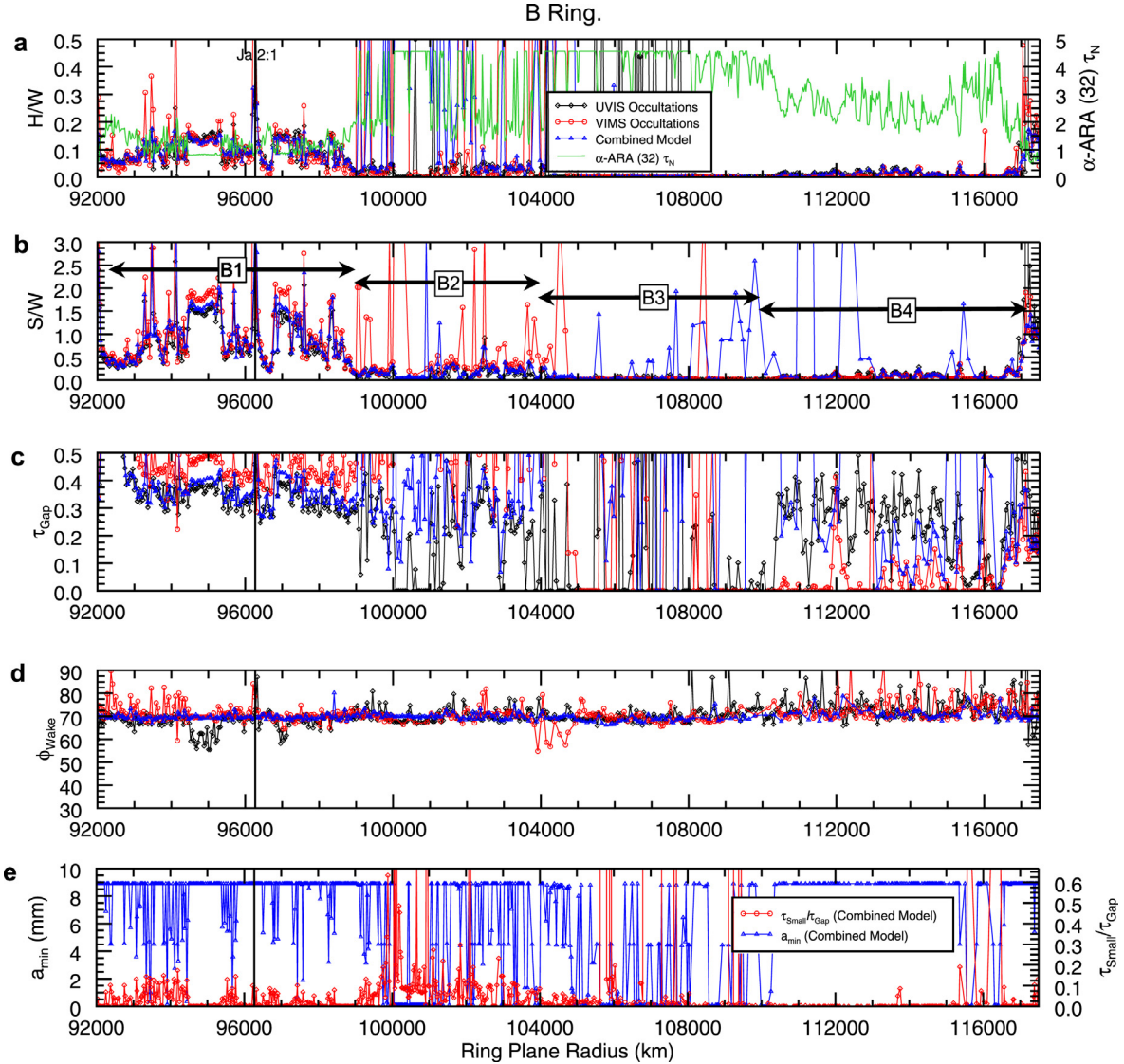


Fig. 8. Best-fit H/W (a), S/W (b), τ_{Gap} (c), ϕ_{Wake} (d), and $\tau_{\text{Small}}/\tau_{\text{Gap}}$ and a_{\min} (e) throughout the B Ring. The normal optical depth profile from the occultation of the bright star α -Arae (32) is overplotted (solid green). The optical depth is indistinguishable from infinity at $\tau_N \sim 4.5$, where the profile is flat. This illustrates the regions within the B ring where wake parameters are poorly constrained since the ring plane is opaque to nearly all of the VIMS and UVIS occultations. (For interpretation of the references to color in this figure legend, the reader is referred to the web version of this article).

(exterior to the Janus 5:4 inner Lindblad resonance). The fractional difference in best-fit gap optical depth between the VIMS occultations and UVIS occultations increases outward toward the A ring outer edge. The differences in τ_{Gap} are expected since the small particles responsible for the differential diffraction only affect the signal from the gaps between the wakes, which are essentially opaque. Differences between H/W , S/W , and ϕ_{Wake} when using the VIMS occultation data and the UVIS occultation data may be due to the differences in the distribution of viewing geometries and the nature of our idealized model of the wakes as granola-bars. For example, decreasing the separation to width ratio (S/W) of the wakes is equivalent to increasing the gap optical depth over a limited range of ring opening angles, B . Combining both VIMS and UVIS occultation data into a single set with the additional free-parameter, τ_{Small} , expands the range of available viewing geometries and increases the number of occultations which are fit at a given radial location.

The gap optical depth from the VIMS occultations is higher than that for the UVIS occultations in the outer A ring, consistent with the simple model of opaque wakes and a diffuse, low-optical-depth cloud of particles between the wakes that includes

particles smaller than 1 cm. These particles cause VIMS to see less light than if all particles were larger than 1 cm, resulting in a higher VIMS optical depth than UVIS optical depth (which collects all diffracted light and so sees a higher stellar signal than VIMS). When these observations are folded into the granola bar self-gravity wake model, this produces larger τ_{Gap} when VIMS occultations are used (red curve in Fig. 7c) than when only UVIS occultations are used (black curve). However, in the inner part of the A ring this trend reverses: the model returns larger values of τ_{Gap} when using only UVIS occultations than when using only VIMS occultations. This indicates that the simple granola bar model is not fully capturing the geometrical distribution of ring particles in the inner A ring. These discrepancies can be explained, at least in part, by a distribution of gap optical depths rather than a bi-modal distribution of optical depths between gaps and wakes (Colwell et al. 2011, 2012), (Tiscareno et al. 2009), and will be explored in more detail in future work.

All three parameters are notably different in the halos surrounding the strong Janus and Mimas resonances when compared to those in the surrounding regions of the A ring, while individual optical depths measured by stellar occultations do not show

the same variations (except for those occultations at low B angles). These halos extend outward several hundred kilometers from the strongest inner Lindblad resonances (ILRs) and were first observed in the VIMS and UVIS reflectance spectra taken during Cassini's Saturn orbit insertion in July, 2004 (Esposito et al. 2005; Nicholson et al. 2008).

Introducing the free parameter, τ_{Small} , allows us to include occultations from both data sets. Our new five-parameter model (with τ_{Small} , but replacing τ_{Wake} by ∞) reproduces the gap optical depths found by Colwell et al. (2006) using UVIS occultations but with increased sensitivity due to the larger number of data points and increased range of viewing geometries attained by combining both VIMS and UVIS occultations. While the properties of the wakes are notably different in halos surrounding the strong Mimas and Janus ILRs in the A ring, the free parameter τ_{Small} , which represents the excess apparent optical depth measured by VIMS shows no distinguishable variation between the halos and the surrounding ring plane (Fig. 7e). Since τ_{Small} is directly related to the lower cutoff of the particle size distribution (Eq. 7) we find no measurable difference in the sub-cm particle population in the halo regions.

The size of the smallest particles varies across the outer A ring but remains constant throughout the inner and central A ring around 122,000 km–129,000 km where self-gravity wake signatures are most pronounced. At these locations the smallest particles are too large (>8.86 mm) to produce the differential optical depth signal between VIMS and UVIS studied here (Fig. 7e). There is a gradual decline in the size of the smallest particle outward to the outer edge of the A ring, with a_{\min} near the Encke Gap and in the trans-Encke region of 1–4 mm. Our results suggest that a_{\min} may drop below 1 mm in the vicinity of the Keeler Gap and in the trans-Keeler region, though the large number of density waves in the outer A ring complicates the self-gravity wake modeling and leads to higher values of χ^2 there. Self-gravity wakes are not as well modeled by the simple granola bar geometry in that region (Fig. 7e).

Hedman et al. (2007) determined the wake orientation angle, φ_{Wake} , by fitting the transparency measured by five low incidence angle occultations ($B = 9.5^\circ$) of o Ceti at different longitudes to a Gaussian at each radial location throughout the A ring. We find that the model determined φ_{Wake} using VIMS, UVIS or the combined diffraction model fit well with the determination from Hedman et al. (2007) using the o Ceti occultations (Fig. 7d). Since the UVIS occultation set contains a larger number of high incidence angle occultations, the uncertainty in φ_{Wake} is the greatest for this set.

B ring best-fit parameters

Wakes are flatter and less widely separated in B1 and B2 ($\sim 92,000$ – $104,000$ km) than in the central A ring. Gap optical depths are significantly higher using VIMS occultations and the original four-parameter model of Colwell et al. (2007) than when using only UVIS occultations (Fig. 8c). We find $\varphi_{\text{Wake}} \sim 70^\circ$ and nearly constant across the B1 and B2 regions from $\sim 92,000$ km – $104,000$ km from Saturn's center, contrary to Colwell et al. (2007). The differences in best-fit wake parameters which we determine when using only UVIS occultations and those from Colwell et al. (2007) is primarily due to the larger number of observations and wider range of viewing geometries included in our study. In some cases the differences in best-fit gap optical depths are too large to be due to the effects of small particle diffraction. At most radial locations in B3 and B4 ($\sim 104,000$ – $117,500$ km) the ring plane is essentially opaque to nearly all of the VIMS and UVIS occultations at incidence angles below $B \sim 60^\circ$ and the best-fit wake parameters determined by our 5 parameter model are poorly constrained. We

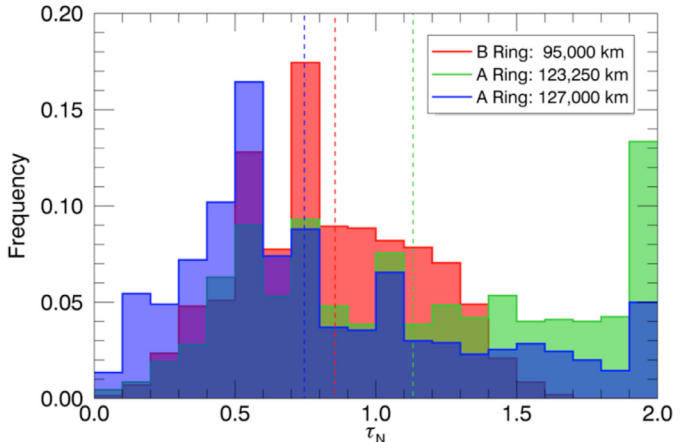


Fig. 9. Truncated normal optical depth distributions for the high incidence occultation of β -Centauri (rev 77) between 126,995 km and 127,005 km (dashed blue line) with a mean normal optical depth of ~ 0.61 , between 123,245 km – 123,255 km (dashed green line) with a mean normal optical depth of ~ 1.12 , and between 94,995 km and 95,004.7 km (dashed red line) with a mean optical depth of ~ 0.85 . The blue histogram shows a complicated distribution with bimodal characteristics indicating a better fit of our (bimodal) optical depth self-gravity wake model in the outer A ring, however the red histogram which shows the distribution of normal optical depths in the B ring has a very different character indicating the necessity of a more robust self-gravity wake model. The radial resolution of β -Centauri (rev 77) was ~ 8.0 m at all three locations. The azimuthal resolution in the frame corotating with the ring particles spanned from ~ 70 – 80 m. Since the self-gravity wakes have a typical wavelength of ~ 50 m and are canted by an angle of 20° from the direction of orbital motion, the self-gravity wakes are resolved in each data point used in these distributions. 1300 optical depth measurements were used to construct each of the three histograms. (For interpretation of the references to color in this figure legend, the reader is referred to the web version of this article).

find no evidence of a sub-cm particle population in the flat lower optical depth region centered at $\sim 95,000$ km with best-fit $a_{\min} \sim 8.86$ mm, consistent with a non-detection. (Fig. 8e).

Limitations of the granola-bar model

Tiscareno et al. (2009) have suggested a trimodal distribution of optical depths in simulated rings consisting of a monodisperse particle size distribution and surface mass density matching estimates for the central A ring. One mode is the relatively opaque wakes which take up only a small fraction of the observed patch of rings, another accounts for the nearly-half of the ring patch that is essentially empty space, and the third accounts for the area between the wakes that is moderately dense with particles. The previous two modes both account for the interwake region such that the area-weighted mean optical depth over which these two modes are sampled represents the gap optical depth, τ_{Gap} which is referred to in this study as well as Colwell et al. (2006, 2007), Hedman et al. (2007) and Nicholson and Hedman (2010). They find that the trimodal nature of the optical depth distribution would only become apparent at extremely low observation angles, (B). Fig. 9 shows normal optical depth distributions from the β -Centauri (rev 77) occultation in both the A and B rings. The B ring distribution of optical depths is qualitatively different than that for the central A ring where self-gravity wakes are most prominent and undisturbed by other dynamical phenomena like density waves or viscous overstabilities. This supports the idea that the simple granola bar geometry is not capturing all of the main characteristics of the small-scale distribution of particles in the B ring.

Because of the non-linear nature of Eq. (8) the model is not equally sensitive to all of the independent parameters. Instead, the model is most sensitive to the parameters S/W , H/W , and τ_{Gap} representing the separation to width ratio of the self-gravity wakes, their height to width ratio, and the interwake optical depth.

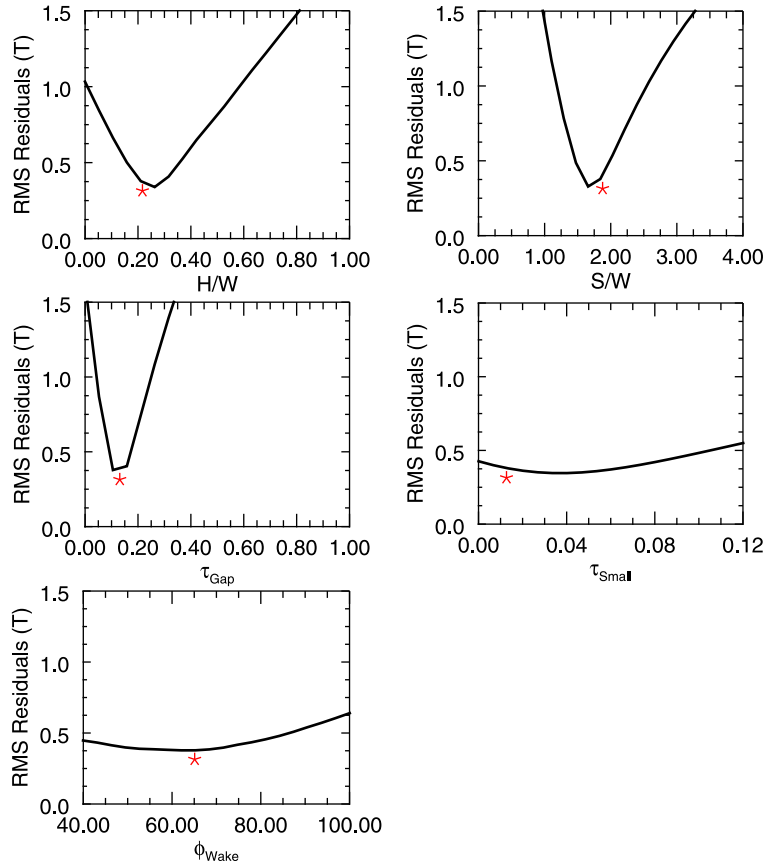


Fig. 10. Cross-sections of the matrix of root-mean-square post-fit residuals in T versus the various wake parameters at a radial location of 133,000 km showing the relative sensitivity of the model over the range of the five free parameters. The best-fit model parameters (asterisks) at this radial location where $H/W \sim 0.22$, $S/W \sim 1.9$, $\tau_{\text{Gap}} \sim 0.13$, $\varphi_{\text{Wake}} \sim 65^\circ$, and $\tau_{\text{Small}} \sim 0.013$ (corresponding to $a_{\min} \sim 4.7$ mm).

Fig. 10 shows cross-sections of the root-mean-square post-fit residuals in T versus each model parameter. The curvature of each cross-section in **Fig. 10** illustrates the ability to pick out a local minimum. [Hedman et al. \(2007\)](#) and [Colwell et al. \(2006\)](#) found similar results for the relative spacing between the wakes. Our new model agrees with the findings from these previous studies but finds less radial variation and smaller wake separations throughout the trans-Encke region, probably due to the larger number of viewing geometries included in this study.

In regions of the ring plane where self-gravity wakes are expected to dominate and where the optical depth varies slowly enough such that the 10-km binned occultation data accurately reflects the radial and azimuthal variations of the ring plane, the reduced chi-squared statistic, χ^2 , is typically ~ 1.00 when using the combined VIMS and UVIS occultation data sets and when weighing the individual occultations by the $1-\sigma$ error in derived transparency. The number of degrees of freedom is the number of modeled occultations less six which varies with radial location but is typically ~ 100 . **Fig. 11** shows χ^2 , which are larger than the Poisson error in individual occultations. Near the strong density waves in the A Ring, where the optical depth varies radially on a scale much smaller than 10 km, the model does not accurately capture the properties of the self-gravity wakes or the photometric properties of the ring plane which is shown by the significantly larger values of χ^2 at these radial locations.

Comparisons between model-determined transparency, T_{Comp} , and measured transparency, T_{Measured} , show good agreement over a wide range of azimuth angles and ring opening angles (except at extremely low occultation elevation angles where the ring plane is nearly opaque). Model predictions of the transparency are also able

to fit the variation in measured transparency over a wide range of azimuth angles, φ and elevation angles, B (**Fig. 13**).

Uncertainties in the model-derived values of a_{\min} are functions of uncertainties in the model-fit parameter τ_{Small} , as well as the uncertainties in the values of q and n_0 , which were derived by [Zebker et al. \(1985\)](#) from the inversion of the near-forward scattered 3.6 cm (X-band) signal and modeling of the 3.6 cm (X-band) and 13 cm (S-band) differential optical depth as a power-law distribution over $0.1 \text{ cm} < a < 1 \text{ m}$. **Fig. 12** (a, b) shows the variation of a_{\min} as a function of τ_{Small} and q (a) and as a function of τ_{Small} and n_0 (b).

5. Discussion

Using the rectangular cross-section “granola bar” wake model of [Colwell et al. \(2006, 2007\)](#) we find best-fit gap optical depths in the outer half of the A ring which are larger by a few percent when fitting VIMS occultations than when fitting UVIS occultations. By including a new free parameter, τ_{Small} , that represents the additional apparent optical depth observed by VIMS occultations due to light diffracted out of the VIMS field of view by small particles in the gaps between opaque self-gravity wakes we recover wake parameters for the combined VIMS and UVIS data that are generally consistent with results from previous studies ([Colwell et al. 2006, 2007](#); [Hedman et al. 2007](#), [Nicholson and Hedman 2010](#)). However, the much larger number of occultations included in our study at a wider range of viewing geometries allow us to more accurately determine the characteristics of self-gravity wakes throughout the ring system.

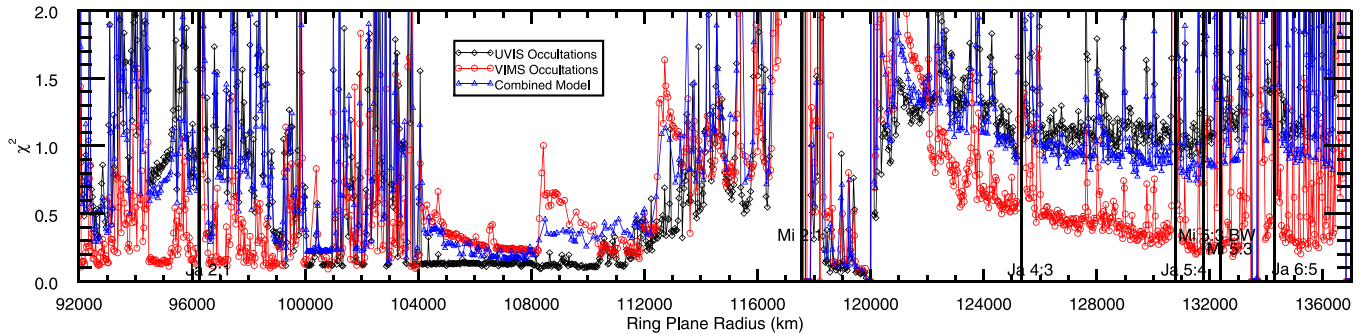


Fig. 11. The reduced chi-squared statistic, χ^2 , determined using the granola-bar model of Colwell et al. (2006, 2007) and UVIS occultations (black), VIMS occultations (red), and the “Combined” diffraction model, combining both VIMS and UVIS occultations (blue). In B2 and B3 the model is over-constraining the data since we have many occultations but the ring plane is essentially opaque to all but occultations of the brightest stars. The squared differences in measured and model-derived transparencies were weighted by their individual errors in counting statistics given by Eqs. (7 and 8) and by the number of degrees of freedom following Eq. (13). The number of model parameters is five for the granola bar model (black, red) and six for the “Combined” model (blue). The number of modeled occultations varies radially but is typically on the order of 100 in the A ring. (For interpretation of the references to color in this figure legend, the reader is referred to the web version of this article).

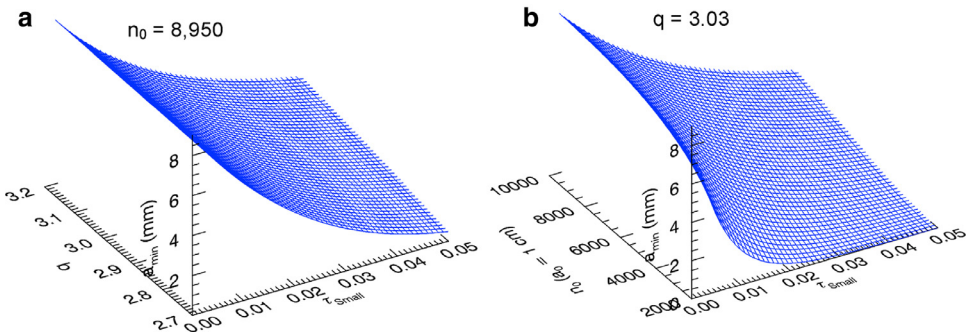


Fig. 12. (a) a_{\min} versus τ_{Small} and q with n_0 fixed and (b) a_{\min} versus τ_{Small} and n_0 with q fixed. n_0 and q are fixed to their respective values between 133,930–136,359 km, in the trans-Encke region.

In the A ring, we find highly flattened wakes with a height to width ratio (H/W) which increases radially outward from $\sim 124,000$ km to the Encke gap. The separation of the wakes increases with the height such that S/H is ~ 7.0 . In the halo regions surrounding the strong resonances with Janus and Mimas, we find slightly thicker and more widely separated self-gravity wakes, potentially due to the diffusion of small (but $>\sim 1$ cm) particles out of resonance. Between 122,000 and 124,000 the measured slant path optical depths are indistinguishable from infinity for all but the brightest stars or occultations at high B angles or occultations where the line of sight to the star is nearly parallel to the wakes. Here we find highly flattened and closely spaced wakes in locations where the model is able to fit the measured optical depths well. The combined VIMS/UVIS model produces best-fit gap optical depths, τ_{Gap} , that are consistent with Colwell et al. (2006) throughout the A ring. The halo regions are apparent in the gap optical depths with increases of $\sim 30\%$ (Janus 5:4) in the gap optical depth farther from the location of the resonance. The orientation of the wakes relative to the direction of orbital motion, $(90^\circ - \varphi_{\text{wake}})$, varies from about 20° – 25° consistent with theory and the results from Colwell et al. (2006) and Hedman et al. (2007).

In the A ring, the best-fit values of τ_{Small} indicate an absence of sub-cm particles out to $\sim 132,500$ km. From this distance outward, we find an increasing population of sub-cm particles with a minimum particle size of ~ 4 mm near the outer edge of the Encke gap which drops to ~ 1 mm near the outer edge of the A ring. This is consistent with ground-based measurements (French and Nicholson, 2000) as well as dynamical theory which predicts smaller particle sizes in regions where random velocities are increased by satellite perturbations. This explanation has also been used to explain the slightly elevated optical depths of the halos surrounding the strong A ring resonances, however we do not see evidence of

significant increases in the number of sub-cm particles in the halos. We do find an increase in the height, separation, and gap optical depth in the halos which might be evidence of the disruption of wake formation due to increased interparticle velocities that are stirred by mass aggregates whose formation is triggered at the resonance (Esposito et al. 2012). Becker et al. (2015), who studied the diffraction of starlight at ring edges from stellar occultations measured by UVIS at the A Ring outer edge, found a minimum particle radius of ~ 4.5 mm using a power law slope of $q \sim 3.2$ and virtually no sub-cm particles at the Encke gap outer edge. Analysis of the diffraction of sunlight measured by VIMS solar occultations carried out by Harbison et al. (2013) also accounted for the presence of self-gravity wakes by using the wake properties determined by Hedman et al. (2007). They found a significant sub-mm particle population throughout the A ring when using $q \sim 2.75$, determined by French and Nicholson, (2000). This suggests using $q > 3$ could bring VIMS solar occultation results into agreement with ours.

Throughout the B ring, the measured normal optical depth is indistinguishable from infinity for nearly all of the UVIS and VIMS occultations. The consequences of the lack of useable data points are poor constraints on the wake parameters and particle sizes except in the lower optical depth region in B1 centered on 95,000 km. Here we find a height to width ratio of $H/W \sim 0.20$ and gaps which are nearly 1.5 times larger than the wake width. The wake orientation is $\sim 70^\circ$ from the outward radial direction and gap optical depths are consistent with that of the Trans-Encke region, $\tau_{\text{Gap}} \sim 0.3$. We find no significant population of sub-cm particles in this region. We find more flattened and less widely separated wakes in B1, B2, and the Trans-Encke Region compared to previous studies by Colwell et al. (2006, 2007), Hedman et al. (2007), and Nicholson and Hedman, (2010) by including more optical depth profiles at a much wider range of viewing geometries.

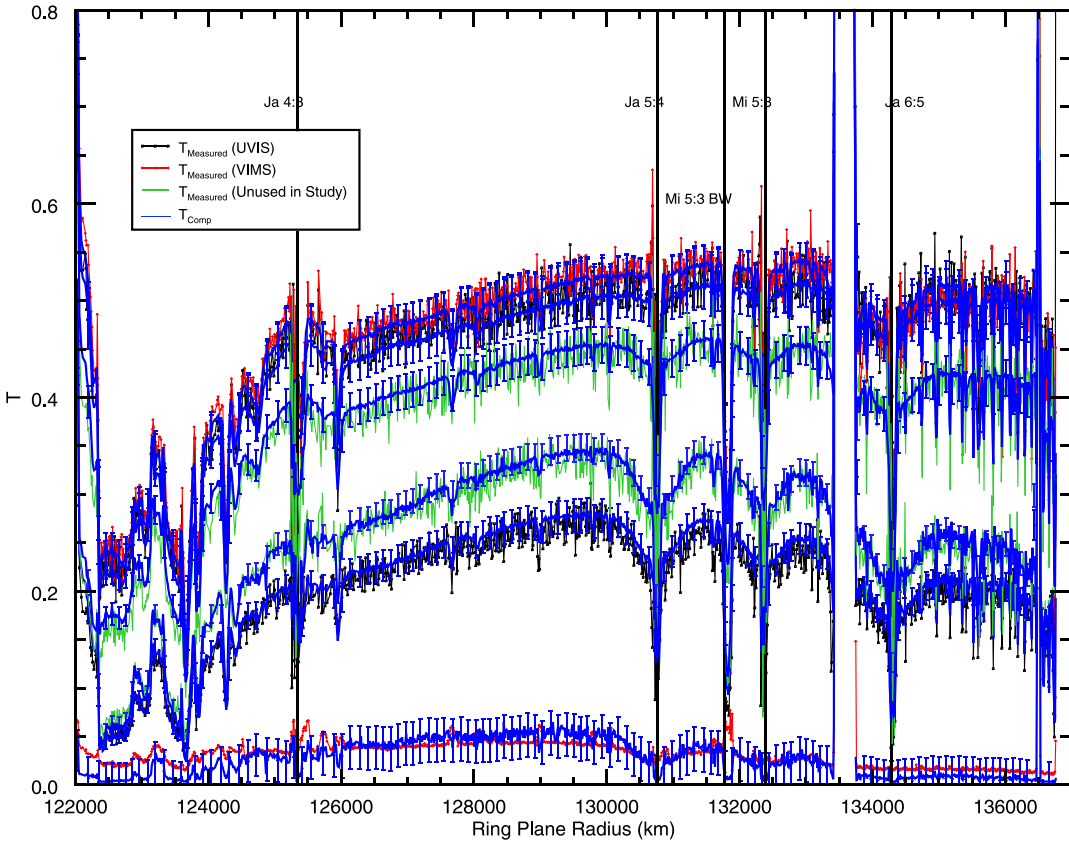


Fig. 13. Comparisons between measured transparency, T_{Measured} , and model determined transparency, T_{Comp} , for two UVIS occultations (black) and two VIMS occultations (red). The model-computed transparencies using the best-fit self-gravity wake parameters and minimum particle radius, combined with the occultation viewing angles produce T_{Comp} (blue). The 2 UVIS occultations are λ -Ceti (28) Ingress (lower observed transparency) at $B = 15.4^\circ$, $53^\circ < \varphi < 259^\circ$, and δ -Persei (41) Ingress (higher observed transparency) at $B = 54.0^\circ$, $53^\circ < \varphi < 241^\circ$. The 2 VIMS occultations are α -Ceti (9) Egress (lower observed transparency) at $B = 3.5^\circ$, $278^\circ < \varphi < 318^\circ$, and γ -Crucis (73) Ingress at $B = 62.3^\circ$, $223^\circ < \varphi < 232^\circ$. T_{Comp} error bars (blue) represent the root-mean-square post-fit residuals in T and are an estimate of all of the systematic errors in the model which are strongly correlated for points along the same occultation profile. Errors in T_{Measured} are generally smaller than the plot symbols. Plot symbols and error bars are shown for every 10th data point. Additionally the transparencies measured by two UVIS occultations which were not included in the model, α -Lyrae (206) Egress at $B = 35.2^\circ$ and α -Virginis (211) Egress at $B = 17.3^\circ$, (green) and predicted transparencies (blue) based on the best-fit wake parameters. (For interpretation of the references to color in this figure legend, the reader is referred to the web version of this article).

The determination of the slope of the power law size distribution, q , is impossible to obtain with our model and only two wavelengths. Future studies incorporating additional occultation data at a third wavelength would allow us to measure q in regions where the optical depth is complicated by the presence of self-gravity wakes and therefore improve the accuracy of the size distribution at sub-cm length scales.

Acknowledgments

This material is based upon work supported by the National Aeronautics and Space Administration under Grant No.

NNX10AF20G issued through the Cassini Data Analysis Program, and by the Cassini project and the UVIS team. We are indebted to the Cassini Rings Target Working Team and Rings Working Groups whose support for, and integration of, these observations has made this research possible. We also thank Stuart Pilorz and an anonymous reviewer who's comments have greatly improved the quality of this paper.

Appendix

See Table A.1.

Table A.1

UVIS and VIMS stellar occultations used in this study. Some of the occultations cut a chord across the rings and sampled the same radial location at two different longitudes around the rings. The ingress and egress sections of occultations are labeled “I” and “E”, respectively.

Star		Rev		Date	Time [†]	R_{\min} (km)	R_{\max} (km)	B	φ_{\min}	φ_{\max}	I_0 (Hz) [†]
UVIS	Occultations										
α	Arae	36	I	4-Jan-07	21:16:15	70,897	113,927	54.4	3.4	54.9	39,866
α	Arae	32	I	9-Nov-06	20:10:23	61,332	139,762	54.4	276.5	280.9	39,709
α	Arae	33	I	21-Nov-06	18:52:31	65,875	145,335	54.4	276.6	280.8	39,010
α	Arae	63	E	1-Apr-08	9:49:51	73,261	141,541	54.4	95.8	112.3	30,419

(continued on next page)

Table A.1 (continued)

Star UVIS Occultations	Rev	Date	Time [†]	R _{min} (km)	R _{max} (km)	B	φ _{min}	φ _{max}	I ₀ (Hz) [†]	
α Arae	65	E	20-Apr-08	15:01:19	125,009	143,829	54.4	110.4	112.9	30,365
α Arae	79	I	4-Aug-08	2:52:47	94,195	157,525	54.4	0.1	360.0	12,546
α Arae	85	E	30-Aug-08	0:31:59	93,510	157,460	54.4	50.5	306.2	25,665
α Arae	85	I	17-Sep-08	8:08:31	93,510	160,520	54.4	0.0	359.9	25,732
α Arae	86	E	23-Sep-08	14:15:27	93,407	160,087	54.4	50.6	316.4	11,300
α Arae	90	E	24-Oct-08	4:05:19	92,106	156,626	54.4	50.0	106.7	10,681
α Arae	90	I	24-Oct-08	1:02:23	92,106	160,526	54.4	0.1	360.0	10,321
α Arae	96	E	9-Dec-08	7:38:07	108,169	155,129	54.4	46.9	94.1	10,161
α Arae	96	I	9-Dec-08	4:53:19	108,169	150,829	54.4	1.7	46.9	10,145
α Arae	98	E	25-Dec-08	9:09:51	110,536	152,106	54.4	42.4	86.3	9167
α Arae	98	I	25-Dec-08	5:42:55	110,536	154,506	54.4	0.0	360.0	8873
α Arae	105	E	7-Mar-09	21:07:10	93,917	143,357	54.4	39.3	88.6	5701
α Arae	105	I	7-Mar-09	15:37:02	93,917	163,817	54.4	0.1	360.0	5949
α Crucis	92	I	7-Nov-08	18:35:11	77,557	155,707	68.2	125.0	181.7	261,142
α Crucis	100	E	12-Jan-09	17:31:42	114,050	149,430	68.2	83.5	124.1	219,486
α Crucis	100	I	12-Jan-09	13:31:10	114,050	149,130	68.2	124.2	164.8	221,498
α Leonis	9	I	8-Jun-05	4:05:36	114,150	204,690	9.5	10.7	67.9	48,113
α Leonis	9	I	8-Jun-05	6:01:36	114,149	131,529	9.5	98.4	278.4	43,866
α Scorpis	13	I	20-Aug-05	10:50:56	101,173	155,723	32.2	80.0	208.5	14,872
α Scorpis	13	E	20-Aug-05	12:45:36	101,173	146,563	32.2	105.9	155.0	14,767
α Virginis	8	E	13-May-05	5:38:24	118,978	141,708	17.3	82.2	115.3	524,941
α Virginis	8	I	21-May-05	5:05:20	118,978	141,928	17.3	36.0	150.1	497,707
α Virginis	30	I	12-Oct-06	6:54:23	64,010	151,520	17.3	219.8	266.4	548,086
α Virginis	34	E	3-Dec-06	3:05:51	74,536	160,086	17.3	282.4	344.7	537,390
α Virginis	34	I	3-Dec-06	1:58:07	74,536	153,626	17.3	220.9	282.0	525,940
α Virginis	116	I	11-Aug-09	14:25:02	103,057	144,537	17.3	241.8	244.9	84,529
β Centauri	77	E	21-Jul-08	5:00:15	73,267	143,417	66.7	34.6	54.4	310,158
β Centauri	77	I	20-Jul-08	22:25:03	73,333	144,873	66.7	264.4	282.9	300,268
β Centauri	78	E	28-Jul-08	5:21:35	58,470	145,000	66.7	23.7	54.8	292,091
β Centauri	81	I	18-Aug-08	11:11:59	72,828	151,668	66.7	267.6	294.5	277,615
β Centauri	85	I	16-Sep-08	22:54:55	73,111	143,391	66.7	269.5	295.3	540,648
β Centauri	89	I	16-Oct-08	8:58:07	71,853	141,863	66.7	269.9	296.4	255,803
β Centauri	92	E	8-Nov-08	6:01:35	50,676	154,546	66.7	42.7	59.1	239,154
β Centauri	96	I	8-Dec-08	16:19:43	72,455	155,315	66.7	264.8	288.6	224,254
β Centauri	102	I	31-Jan-09	19:07:42	73,242	143,482	66.7	248.3	250.7	187,927
β Centauri	104	E	22-Feb-09	23:00:14	68,934	131,964	66.7	94.7	134.8	184,324
β Centauri	104	I	22-Feb-09	15:30:06	68,934	147,264	66.7	134.8	220.0	183,037
β Crucis	98	I	24-Dec-08	7:29:03	58,104	154,664	65.2	157.3	202.6	141,348
β Hydreae	60	I	27-Feb-08	21:45:51	121,735	162,245	38.6	173.7	183.2	1212
β Librae	124	E	11-Jan-10	14:01:34	115,070	123,480	15.8	221.6	237.0	1438
β Lupi	57	I	26-Jan-08	19:01:35	119,418	148,128	49.6	226.1	231.9	77,163
β Lupi	114	I	12-Jul-09	5:25:50	118,474	144,814	49.6	186.8	217.4	12,727
β Persei	42	I	8-Apr-07	15:34:55	84,460	149,650	47.4	227.8	230.8	10,156
β Sagittarii	41	E	9-Dec-06	20:50:23	127,360	141,930	46.3	39.0	119.2	3362
β Sagittarii	41	I	20-Mar-07	8:53:35	127,360	135,480	46.3	18.2	122.2	3133
χ Centauri	39	I	25-Feb-07	19:33:19	98,599	148,409	47.6	159.9	183.9	13,369
δ Aquarii	8	E	21-May-05	20:49:36	60,687	169,877	12.2	106.8	131.4	1511
δ Lupi	57	I	26-Jan-08	20:43:27	114,918	147,938	47.0	259.4	260.4	49,398
ε Persei	36	E	30-Dec-06	16:03:59	66,531	140,881	54.0	65.7	68.3	14,522
ε Persei	37	I	15-Jan-07	13:16:47	60,043	142,563	54.0	258.1	281.1	14,484
ε Persei	39	I	18-Feb-07	17:36:15	55,504	143,264	54.0	257.8	284.1	6674
ε Persei	41	I	23-Mar-07	11:47:27	49,259	149,719	54.0	232.8	240.6	12,981
ε Persei	60	I	2-Mar-08	6:39:59	54,974	146,194	54.0	274.5	283.9	6138
ε Cassiopei-ae	104	E	27-Feb-09	14:10:06	111,694	151,504	70.0	111.7	154.4	2407
γ Cassiopei-ae	104	I	27-Feb-09	9:45:34	111,694	154,544	70.0	154.6	198.6	2380
γ Lupi	36	E	3-Jan-07	8:52:47	63,450	148,820	51.0	36.6	48.3	34,337
γ Lupi	37	E	21-Nov-06	19:49:19	99,479	142,919	51.0	0.0	360.0	33,541
ε Piscis Austrini	38	I	27-Jan-07	13:08:15	82,194	114,614	23.7	255.9	299.3	2638
η Lupi	34	E	3-Dec-06	13:24:47	106,848	143,818	44.5	0.0	360.0	48,284
η Lupi	34	I	3-Dec-06	13:24:47	106,848	143,818	44.5	0.0	360.0	48,284
γ Arae	37	I	22-Jan-07	1:04:31	121,466	147,926	61.0	245.6	251.2	27,227
γ Cassiopei-ae	64	I	11-Apr-08	12:11:27	71,732	119,572	66.3	0.1	359.9	107,673
ι Cassiopei-ae	100	E	15-Jan-09	11:19:58	72,440	140,350	66.3	66.0	86.4	29,393
ι Gruis	41	E	21-Mar-07	14:37:35	91,528	142,208	35.1	192.9	242.9	8356
ι Gruis	41	I	21-Mar-07	10:54:55	91,528	145,938	35.1	243.1	294.4	8274
ι Lupi	30	E	13-Oct-06	1:40:15	83,062	141,032	47.4	102.7	157.0	82,558
γ Lupi	30	I	12-Oct-06	23:35:27	83,062	94,562	47.4	157.3	185.9	82,191
γ Lupi	57	I	26-Jan-08	22:22:39	135,462	148,192	47.4	261.8	262.3	65,761

(continued on next page)

Table A.1 (continued)

Star UVIS Occultations	Rev	Date	Time [†]	R _{min} (km)	R _{max} (km)	B	φ _{min}	φ _{max}	I ₀ (Hz) [‡]	
ι Pegasi	36	E	28-Dec-06	16:37:35	102,296	146,776	20.3	55.8	185.8	75,532
γ Pegasi	36	I	29-Dec-06	8:04:47	102,295	178,155	20.3	156.6	336.6	76,776
ι Centauri	56	E	14-Jan-08	17:40:47	131,855	141,185	42.7	77.5	80.0	801
ι Centauri	57	E	26-Jan-08	15:35:27	128,120	144,630	42.7	76.5	80.8	903
κ Centauri	35	E	16-Dec-06	20:34:39	68,853	146,153	48.5	76.5	108.8	48,936
λ Centauri	36	I	2-Jan-07	14:24:31	63,523	156,353	48.5	237.8	250.0	45,538
λ Centauri	42	E	26-Mar-07	3:03:11	114,713	127,803	48.5	115.3	231.3	42,371
λ Centauri	42	I	2-Apr-07	7:18:07	114,713	142,133	48.5	142.4	213.8	42,447
λ Ceti	28	I	9-Sep-06	5:53:51	74,327	143,987	15.4	258.5	304.1	2723
μ Scorpii	29	E	26-Sep-06	21:07:43	88,478	143,778	41.7	136.4	189.0	294,809
μ Scorpii	44	I	9-May-07	11:05:51	69,544	141,044	41.7	211.1	244.4	262,096
μ Centauri	113	I	26-Jun-09	19:06:38	75,975	155,765	48.7	236.2	240.6	4938
ψ Centauri	38	I	6-Feb-07	22:07:11	96,419	150,149	44.3	243.8	260.3	4818
ψ Centauri	38	I	6-Feb-07	22:07:11	96,419	150,149	44.3	243.8	260.3	4818
σ Sagittarii	11	I	14-Jul-05	22:51:12	85,972	146,902	29.1	221.9	248.8	119,296
θ Arae	40	E	26-Feb-07	12:58:39	130,042	136,072	53.9	17.1	291.2	12,623
θ Arae	40	I	1-Mar-07	16:33:51	130,042	146,832	53.9	0.0	360.0	12,619
θ Arae	41	E	19-Mar-07	13:37:35	63,681	152,201	53.9	63.8	89.4	12,589
ζ Orionis	47	E	28-Jun-07	4:39:01	78,770	137,730	2.7	99.3	106.5	184,281
ζ Centauri	60	I	29-Feb-08	16:06:23	66,648	146,488	53.6	221.1	231.2	111,287
ζ Centauri	62	E	22-Mar-08	11:15:27	63,689	145,059	53.6	67.0	77.3	110,896
ζ Centauri	112	I	12-Jun-09	10:10:38	71,486	143,186	53.6	236.6	241.2	19,753
ζ Ophiuchi	26	I	25-Jul-06	0:04:31	120,941	149,211	16.2	116.6	126.7	15,211
ζ Persei	42	E	4-Apr-07	17:16:15	132,811	137,931	38.0	328.7	344.0	5412
ζ Persei	42	I	4-Apr-07	18:10:54	132,810	134,680	38.0	138.0	318.2	5247
<i>VIMS Occultations</i>										
CW Leonis	70	E	3-Jun-08	15:18:47	105,669	140,869	11.4	226.9	268.0	209,242
CW Leonis	70	I	3-Jun-08	13:30:04	105,669	148,979	11.4	268.7	313.2	207,128
CW Leonis	74	E	2-Jul-08	01:43:00	112,475	163,055	11.4	222.1	268.1	78,394
CW Leonis	74	I	2-Jul-08	00:04:16	112,475	147,365	11.4	268.9	308.8	75,485
γ Gruis	73	I	22-Jun-08	17:46:04	61,838	144,543	62.3	223.4	232.2	16,653
R Cassio-peiae	65	I	21-Apr-08	00:20:26	63,076	138,306	56.0	170.0	196.3	35,495
R Cassio-peiae	106	I	22-Mar-09	20:28:09	80,343	145,943	56.0	127.7	180.8	67,278
R Hydrael	36	I	1-Jan-07	16:07:55	66,112	150,662	29.4	228.1	288.0	174,117
R Hydrael	41	I	29-Mar-07	05:44:57	91,473	144,193	29.4	223.5	234.2	56,166
R Hydrael	42	I	15-Apr-07	16:22:01	119,702	140,762	29.4	138.2	156.4	58,333
R Leonis	60	E	3-Mar-08	02:25:31	126,100	145,160	9.5	235.9	265.3	232,346
R Leonis	60	I	3-Mar-08	01:45:10	126,100	148,120	9.5	266.0	297.2	236,369
R Leonis	63	E	3-Apr-08	15:56:23	114,775	174,105	9.5	217.7	266.2	193,827
R Leonis	63	I	3-Apr-08	14:52:58	114,775	146,135	9.5	266.9	304.7	192,714
R Leonis	75	E	9-Jul-08	07:44:17	104,182	158,632	9.5	219.6	268.1	148,323
R Leonis	77	E	23-Jul-08	06:39:27	108,286	159,336	9.5	221.3	268.2	156,472
R Leonis	77	I	23-Jul-08	13:34:45	108,286	148,316	9.5	268.9	311.6	153,849
R Leonis	86	E	27-Sep-08	12:25:45	127,261	152,311	9.5	234.9	267.9	339,526
R Leonis	86	I	27-Sep-08	13:34:45	127,261	167,451	9.5	268.5	308.8	341,977
R Leonis	87	E	4-Oct-08	12:25:45	128,141	146,311	9.5	239.4	267.9	160,957
R Leonis	87	I	4-Oct-08	16:51:46	128,141	149,281	9.5	268.7	299.2	159,021
RS Cancri	80	E	13-Aug-08	15:21:36	78,005	143,135	30.0	207.8	264.6	158,050
RS Cancri	80	I	13-Aug-08	05:34:46	78,005	144,265	30.0	265.4	322.5	163,945
RS Cancri	85	E	19-Sep-08	03:56:08	81,122	145,602	30.0	208.8	264.7	184,064
RS Cancri	85	I	18-Sep-08	07:42:57	81,122	144,172	30.0	265.7	321.2	163,560
RS Cancri	87	E	3-Oct-08	06:11:02	82,507	143,887	30.0	210.0	264.9	173,237
RS Cancri	87	I	3-Oct-08	10:48:27	82,507	144,817	30.0	265.7	320.7	171,884
RS Cancri	92	I	10-Nov-08	09:20:05	111,367	142,677	30.0	265.2	303.7	120,354
α Auriga-e	34	I	2-Dec-06	19:37:22	66,568	148,138	50.9	283.4	300.3	214,438
α Auriga-e	41	I	23-Mar-07	18:35:19	71,915	143,195	50.9	297.9	348.6	101,224
α Auriga-e	110	E	9-May-09	04:46:24	95,406	145,626	50.9	34.9	83.6	132,375
α Auriga-e	110	I	9-May-09	01:05:09	95,406	144,806	50.9	0.1	360.0	164,134
α Orionis	26	I	9-Sep-06	01:08:32	111,919	139,019	11.7	313.9	325.2	502,498
α Scorpii	29	I	26-Sep-06	15:15:14	94,694	149,194	32.2	274.2	300.0	366,541
α Scorpii	55	E	3-Jan-08	03:07:00	119,788	141,948	32.2	54.2	67.9	386,389
β Pegasi	104	I	26-Feb-09	00:35:24	73,094	150,394	31.7	214.2	233.7	154,893
\circ Ceti	8	E	24-May-05	12:10:55	114,965	167,765	3.5	277.9	324.4	543,005
\circ Ceti	8	I	24-May-05	16:38:04	114,965	162,465	3.5	232.7	277.2	524,742
\circ Ceti	9	E	11-Jun-05	14:17:08	125,925	165,525	3.5	277.9	318.1	506,249
\circ Ceti	9	I	11-Jun-05	10:20:59	125,925	155,595	3.5	241.6	277.2	501,828
\circ Ceti	10	E	29-Jun-05	14:17:08	132,020	174,000	3.5	277.9	318.2	594,915
\circ Ceti	10	I	29-Jun-05	10:20:59	132,020	155,170	3.5	245.8	277.2	597,353

[†] Beginning time of the occultation (UT).[‡] The unocculted star signal, I₀, reported above is the photon count rate in Hz for UVIS occultations, while for VIMS occultations I₀ represents the data number (DN) per second.

References

- Becker, T.M., Colwell, J.E., Esposito, L.W., et al., 2015. Characterizing the particle size distribution of Saturn's A ring with cassini UVIS occultation Data. *Icarus* doi:10.1016/j.icarus.2015.11.001.
- Bodrova, A., Schmidt, J., Spahn, F., et al., 2012. Adhesion and collisional release of particles in dense planetary rings. *Icarus* 218 (1), 60–68. doi:10.1016/j.icarus.2011.11.011.
- Brown, R.H., Barnes, K.H., Bellucci, G., et al., 2004. The cassini visual and infrared mapping spectrometer investigation. *Space Sci. Rev.* 115, 111–168.
- Brilliantov, N., Krapivsky, P.L., Bodrova, A., et al., 2015. Size distribution of particles in Saturn's rings from aggregation and fragmentation. *PNAS* 112 (31), 9536–9541.
- Camichel, H., 1958. Mesures photométriques de Saturne et de son anneau. *Ann. Astrophys.* 21, 231–242.
- Colombo, G., Goldreich, P., Harris, A.W., 1976. Spiral structure as an explanation for the asymmetric brightness of Saturn's A ring. *Nature* 264, 344–345.
- Colwell, J.E., Esposito, L.W., Sremčević, M., 2006. Gravitational wakes in Saturn's A ring measured by stellar occultations from Cassini. *Geophys. Res. Lett.* 33. doi:10.1029/2005GL025163, L07201.
- Colwell, J.E., Esposito, L.W., Sremčević, M., et al., 2007. Self-gravity wakes and radial structure of Saturn's B ring. *Icarus* 190, 127–144. doi:10.1016/j.icarus.2007.03.018.
- Colwell, J.E., Esposito, L.W., Pettis, D., et al., 2010. Cassini UVIS stellar occultation observations of Saturn's Rings. *Astron. J.* 140, 1569–1578. doi:10.1088/0004-6256/140/6/1569.
- Colwell, J.E., Jerousek, R.G., Cooney, J.H., 2011. Revisiting the self-gravity wakes granular bar model, more data, more parameters. In: Proceedings of Cornell Rings Workshop July 28th, 2011.
- Colwell, J.E., Jerousek, R.G., Esposito, L.W., 2012. Variations of self-gravity wake structures across Saturn's rings. In: Proceedings of American Geophysical Union Fall Meeting, pp. P51B–2031.
- Colwell, J.E., Horn, L.J., Lane, A.L., et al., 1990. Voyager photopolarimeter observations of uranian ring occultations. *Icarus* 83, 102–125. doi:10.1016/0019-1035(90)90009-X.
- Cuzzi, J.N., 1985. Rings of Uranus: Not so thick, not so black. *Icarus* 63, 312–316.
- Dones, L., Proco, C.C., 1989. Spiral density wakes in Saturn's A ring? *Bull. Seismol. Am. Astron. Soc.* 21, 929.
- Dones, L., Cuzzi, J.N., Showalter, M.R., 1993. Voyager photometry of Saturn's A ring. *Icarus* 105, 184–215.
- Dunn, D.E., Molnar, L.A., Niehof, J.T., et al., 2004. Microwave observations of Saturn's rings: anisotropy in directly transmitted and scattered Saturnian thermal emission. *Icarus* 171, 183–198.
- Esposito, L.W., Barth, C.A., Colwell, J.E., et al., 2004. The Cassini ultraviolet imaging spectrograph investigation. *Space Sci. Rev.* 115, 299–361.
- Esposito, L.W., Albers, N., Meinke, B.K., et al., 2012. A Predator-Prey Model for Moon-triggered Clumping in Saturn's Rings. *Icarus* 217, 103–114. doi:10.1016/j.icarus.2011.09.029.
- Esposito, L.W., Colwell, J.E., Larsen, K., et al., 2005. Ultraviolet imaging spectroscopy shows an active Saturnian system. *Science* 308, 1251–1255. doi:10.1126/science.1105606.
- French, R.G., Nicholson, P.D., 2000. Saturn's rings II. Particle sizes inferred from stellar occultation data. *Icarus* 145, 502–523. doi:10.1006/icar.2000.6357.
- Gehrels, T., Esposito, L.W., 1981. Pioneer fly-by of Saturn and its rings. *Adv. Space Res.* 1, 67–71.
- Harbison, R.A., Nicholson, P.D., Hedman, M.M., 2013. The smallest particles in Saturn's A and C rings. *Icarus* 226, 1225–1240. doi:10.1016/j.icarus.2013.08.015.
- Hedman, M.M., Nicholson, P.D., Salo, H., et al., 2007. Self-gravity wake structures in Saturn's A ring revealed by Cassini-VIMS. *Astron. J.* 133 (6), 2624–2629.
- Lumme, K., Irvine, W.M., 1976. Azimuthal brightness variations of Saturn's rings. *Astrophys. J.* 204, L55–L57.
- Lumme, K., Esposito, L.W., Irvine, W.M., et al., 1977. Azimuthal brightness variations of Saturn's rings. II. Observations at an intermediate tilt angle. *Astrophys. J.* 216, L123–L126.
- Julian, W.H., Toomre, A., 1966. Non-axisymmetric responses of differentially rotating disks of stars. *Astrophys. J.* 146, 810–830.
- Marouf, E.A., Tyler, G.L., Zebker, H.A., et al., 1983. Particle size distributions in Saturn's rings from Voyager 1 radio occultation. *Icarus* 54, 189–211.
- Maxwell, J.C. 1859. On the stability of Saturn's rings . Reprinted in The Scientific Papers of James Clark Maxwell, 2 Vols. 1890. University of Cambridge Press, Cambridge, London pp. 288–374.
- Nicholson, P.D., French, R.G., Campbell, D.B., et al., 2005. Radar Imaging of Saturn's Rings. *Icarus* 177, 32–62.
- Nicholson, P.D., Hedman, M.M., Clarke, R.N., et al., 2008. A close look at Saturn's rings with Cassini VIMS. *Icarus* 193, 182–212. doi:10.1016/j.icarus.2007.08.036.
- Nicholson, P.D., Hedman, M.M., 2010. Self-gravity wake parameters in Saturn's A and B rings. *Icarus* 206, 410–423 10/1016/j.icarus.2009.07.028.
- Reitsema, H.J., Beebe, R.F., Smith, B.A., 1976. Azimuthal brightness variations in Saturn's rings. *Astron. J.* 81, 209–215.
- Showalter, M.R., Nicholson, P.D., 1990. Saturn's rings through a microscope: Particle size constraints from the Voyager PPS scan. *Icarus* 87, 285–306.
- Salo, H., 1995. Simulations of dense planetary rings: III. Self-gravitating identical particles. *Icarus* 117, 287–312.
- Salo, H., Karjalainen, R., French, R.G., 2004. Photometric modeling of Saturn's rings. II. Azimuthal asymmetry in reflected and transmitted light. *Icarus* 170, 70–90.
- Thompson, W.T., Lumme, K., Irvine, W.M., et al., 1981. Saturn's rings—Azimuthal variations, phase curves, and radial profiles in four colors. *Icarus* 46, 187–200.
- Tiscareno, M.S., Burns, J.A., Hedman, M.M., et al., 2009. The population of propellers in Saturn's A ring. *Astronom. J.* 135, 1083–1091.
- Zebker, H.A., Marouf, E.A., Tyler, G.L., 1985. Saturn's Rings: Particle Size Distributions for Thin Layer Models. *Icarus* 64, 531–548.